Variability in the Characteristics of Precipitation Systems in the Tropical Pacific. Part I: Spatial Structure

HIROHIKO MASUNAGA, TRISTAN S. L'ECUYER, AND CHRISTIAN D. KUMMEROW

Colorado State University, Fort Collins, Colorado

(Manuscript received 22 January 2004, in final form 7 September 2004)

ABSTRACT

Regional and temporal variability in the vertical and horizontal characteristics of tropical precipitating clouds are investigated using the Precipitation Radar (PR) and the Visible and Infrared Scanner (VIRS) on board the Tropical Rainfall Measuring Mission (TRMM) satellite. The present study focuses on the three oceanic regions (west, central, and east Pacific) together with two continental regions for comparison and the two separate time periods (February 1998 and February 2000) under different phases of the El Niño–Southern Oscillation (ENSO) in order to examine regional and ENSO-related variations. The height spectrums of storms are investigated in terms of radar echo-top height and infrared brightness temperature. The variability in the spectrum clearly correlates with the large-scale circulation and its ENSO-related change. On the basis of the height spectrum, storm systems are classified into the four categories of shallow, cumulus congestus, deep stratiform, and deep convective. The deep stratiform and deep convective categories, both of which have very cold cloud tops, are differentiated by radar echo-top heights so that deep convective systems are accompanied with an appreciable amount of large frozen particles aloft. While shallow events are dominant in the probability of occurrence over relatively cold oceans, deep convective systems take their place for warmer sea surface temperatures (SSTs). The turnover occurs at the SST threshold of 28°–29°C for all the oceanic regions and years investigated except the west Pacific in 2000, for which deep convective systems prevail over the entire range of SST. Rain correlation-scale length (RCSL) and cloud correlation-scale length (CCSL) are introduced as statistical indicators of the horizontal scale of storms. While the RCSL is 8–18 km for shallow- and cumulus congestus–type clouds without significant regional and temporal variations, the RCSL and CCSL associated with deep stratiform and deep convective systems consistently exceed 100 km and exhibit a systematic variability. The RCSL and CCSL in the central and east Pacific, particularly, increase significantly in the El Niño year.

1. Introduction

Tropical rainfall systems not only drive the atmospheric circulation dynamically through the release of latent heat, but can also influence the earth's radiation budget through their associated cloud fields. It is therefore crucial to clarify the roles of tropical rain systems in terms of both the dynamical and radiative energy budget for an understanding of the mechanisms governing climate variability. Interactions between dynamical and radiative processes are key factors that connect climate variabilities on different spatial and temporal scales such as the response of the global climate to El Niño–Southern Oscillation (ENSO) events.

The size and height spectra of storms have been extensively studied over decades in order to characterize a wide variety of rain systems, ranging from isolated convection to mesoscale convective system (MCS) in size and from shallow cumulus to deep convection in height. From early studies (López 1976, 1977; Houze and Cheng 1977) to recent ones (e.g., Rickenbach and Rutledge 1998; Johnson et al. 1999), ground radar has been a preferred tool for this purpose. Satellite remote sensing is another useful means especially when a wide area of coverage beyond the scale of a ground-based radar is of interest, as is the case in the present study. To this end, geostationary satellites have been utilized sincethe 1980s to acquire data of homogeneous quality on a synoptic to global scale (Williams and Houze 1987; Machado et al. 1992; Machado and Rossow 1993; Mapes and Houze 1993). Use of a geostationary satellite, however, limits the observational target to clouds, which are only an indirect proxy for precipitation. This could be an obstacle if one wishes to examine dynamical and radiative impacts of storms separately.

Microwave sensors such as the Special Sensor Microwave Imager (SSM/I) aboard the Defense Meteorological Satellite Program (DMSP) satellites provide a more direct means for measuring precipitation from space.

Corresponding author address: Dr. Hirohiko Masunaga, Department of Atmospheric Science, Colorado State University, Fort Collins, CO 80523.
E-mail: masunaga@atmos.colostate.edu

Mohr and Zipser (1996) utilized the SSM/I 85-GHz brightness temperature to study the size spectra of MCSs in various geographical regions across the globe. The 85-GHz ice-scattering signals exhibit a more direct link to rainfall intensity than the cloud signature in infrared radiances, although correlation between ice particles aloft and surface rainfall is not always optimal.

The Tropical Rainfall Measuring Mission (TRMM) satellite was launched in 1997 carrying the Precipitation Radar (PR), the first spaceborne radar measuring rainfall, together with the TRMM Microwave Imager (TMI) and the Visible and Infrared Scanner (VIRS), as well as the Lightning Imaging Sensor (LIS) and the Clouds and Earth's Radiant Energy System (CERES) instrument. The TRMM satellite and PR, in particular, have significantly improved our capability of measuring rainfall from space and have spawned numerous new studies into the characteristics of precipitating cloud systems. Nesbitt et al. (2000) extended the Mohr and Zipser (1996) technique by adding PR information so that precipitation features without ice-scattering signatures could be discriminated from those with ice. Inoue and Aonashi (2000) examined the performance of the infrared technique to detect rainfall using VIRS radiances with the help of PR information. Del Genio and Kovari (2002) employed TMI-identified rainfall to obtain the storm size statistics and discussed the dependence of the rainfall characteristics upon environmental factors. The PR has also facilitated the direct measurement of vertical profiles of precipitation on a global scale. Short and Nakamura (2000) investigated the global distribution of PR echo-top height and found distinct shallow and deep modes in the histogram of echo-top heights. Takayabu (2002) confirmed structural differences in rain profile spectra obtained from PR observations and found that their frequency depended on oceanic/continental and convective/stratiform categories.

Most previous studies mentioned above focused on either precipitation (using a microwave radiometer and/or radar) or cloud temperature (using an infrared imager). The present study, in contrast, aims to understand statistical trends in size and height of both precipitation and associated clouds through a simultaneous analysis of PR and VIRS observations. The VIRS provides infrared brightness temperature as a proxy of cloud-top temperature if clouds are optically thick. Infrared brightness temperature does not necessarily trace the physical temperature of clouds for thin cirrus. In practice, thin cirrus clouds do not have a large impact on the present analysis because only raining clouds identified by collocated PR pixels are taken into account. Cirrus could occasionally overlap with shallow convection beneath. This case is identified by the ill-matched combination of a cold infrared brightness temperature and a low radar echo-top height. The contamination of high clouds is therefore easily avoidable (section 3).

While VIRS infrared radiances outline the cloud top, PR echo-top height represents the maximum altitude for precipitation-size particles. The detectable particle size is limited by the sensitivity of PR or 17 dBZ (TRMM PR Team 2000). Uncertainties in the microphysical properties of frozen hydrometeors such as size, shape, and density lead to a somewhat mixed ability of the PR to detect the actual precipitation height (Masunaga et al. 2002). The combination of VIRS brightness temperature and PR echo-top height is therefore an indicator of the microphysical properties of ice particles aloft, that is, snow, graupel, and hail, as well as the vertical extent of a storm. This paper focuses only on echo-top height without looking further into the detailed structure of rainfall. A well-defined quantity such as echo-top height is sufficient for a robust storm categorization. A separate effort by the authors is underway to retrieve the vertical structure of precipitation from TRMM data.

Combined use of PR and VIRS also provides a means to study the horizontal scale of precipitating cloud systems. The conventional approach to evaluate storm area from satellite data is to count contiguous pixels that have infrared/microwave brightness temperatures lower than a certain threshold. Such methods, however, often encounter limitations resulting from orbit geometry as well as storm morphology. First, the contiguous pixel method identifies separate cells as individual small systems even if they belong to a single larger system. Del Genio and Kovari (2002) found, through visual inspection, that the vast majority of storms defined in this way using TMI pixels were classified as isolated storms instead of belonging to a larger system evident in infrared imagery. Its quantitative impact, however, is unclear when the same method is applied to the finer PR resolution. Arbitrariness in the infrared/microwave threshold can also create an ambiguity in the estimated storm size. Finally, the truncation of storms due to the finite swath width of low earth-orbiting (LEO) satellites can result in an underestimation of storm areas. This effect could be significant for the narrow PR swath (215 km). Nesbitt et al. (2000) estimated that 17% of total rain systems are truncated by the edge of the PR swath, and this rate increases to as much as 82% when MCSs are isolated.

Here, the "correlation-scale length" (CSL) of storms is introduced to evaluate their horizontal scales without the limitations that constrain the contiguous pixel method. The rain (cloud) CSL, defined as the expectation of finding precipitation (a cloud) as a function of distance from a given raining point, reflects the size of a spatially correlated or organized system regardless of contiguity of raining/cloudy areas in it. The CSL has the advantage of not requiring an infrared threshold temperature (except to define storm categories) and is much less susceptible to the effect of finite swath width.

The present paper is dedicated to 1) investigating the height spectra of storm systems in terms of VIRS

brightness temperature and PR echo-top height and defining storm categories based on them, 2) estimating the raining/cloud CSL for each storm category, and 3) examining regional and ENSO-related variations in the vertical and horizontal scales of storms over tropical Pacific oceans. After describing satellite data used in this study in section 2, storms are categorized in terms of infrared brightness temperature and radar echo-top height in section 3. The methodology to derive CSL is introduced and applied to satellite data in section 4. Section 5 is devoted to discussions and comparison to prior studies. The findings are summarized in the final section (section 6).

2. Data

The TRMM satellite, launched in November 1997 (see Kummerow et al. 1998 for detailed descriptions for the TRMM sensors), has a sun-asynchronous orbit with a 35° inclination and an altitude of 350 km (402 km after August 2001). The TRMM PR is a single-frequency (13.8 GHz) radar having horizontal and vertical resolutions of 4.3 km and 0.25 km, respectively, at nadir. The PR sensitivity or minimum detectable echo is 17 dBZ after the system noise is subtracted (TRMM PR Team 2000). Scan angles of PR range between ±17°, resulting in a swath width of 215 km. The VIRS has five channels at the wavelengths of 0.63, 1.6, 3.7, 10.8, and 12.0 μm. The nadir instantaneous field of view (IFOV) is 2.1 km, and the swath width is 720 km for VIRS. The spatial resolutions and swath widths have changed slightly since the TRMM orbit was raised in August 2001. The present study uses data acquired prior to the orbit boost.

The PR 2A23 dataset, one of the TRMM standard products available in the archive, contains "storm height" or the height of PR echo top measured from the ellipsoid representing the earth's surface. The 2A23 storm height is therefore designated as the "echo-top height" of PR in this paper in order not to confuse this term with the VIRS cloud-top temperature, which more closely represents the actual "height" of a given storm. The echo-top height is adopted as is for oceanic rainfall while local elevation is subtracted from it for continental rain. In addition to the echo-top height, the stratiform and convective classification is provided by 2A23. The rain type classification by 2A23 is divided into "stratiform (convective) certain," "probably stratiform (convective)," and "maybe stratiform (convective)" with further subcategories, all of which together are simply designated as stratiform (convective) in this study. VIRS channel-4 (10.8 μm) radiance in the 1B01 dataset is converted to brightness temperature, which is designated as "infrared T_b" or simply "T_b" in this paper.

VIRS pixels are collocated with PR over the inner portion of the VIRS swath that overlaps the narrower PR swath. Adjacent 5×5 (9×9) pixels for PR (VIRS) around the assigned pixel are stored as well in order to take into account the horizontal variability of storms. All orbits during the two separate time periods, February 1998 and February 2000, are analyzed in the present paper. Since tropical climate experienced an El Niño event from 1997 to the middle of 1998, these two months are expected to show a sharp contrast in climate signals between the different phases of ENSO.

This study focuses on three oceanic areas and two continental regions between 10°S and 10°N defined as the west Pacific (105°–150°E), the central Pacific (180°–150°W), and the east Pacific (120°–90°W), as well as the South American and African continents. Although the current study places particular emphasis on the Pacific regions, the two tropical continents are included to contrast the properties of oceanic precipitation systems with those of continental systems. Land and coastal areas are excluded from the analysis for the three Pacific regions. Remote Sensing Systems (RSS) distributes a daily sea surface temperature (SST) dataset derived from TMI (available online at http://www.ssmi.com/tmi/tmi_browse.html). This TRMM-based dataset is adopted to examine the correlation between storm characteristics and SST in section 3 since it minimizes errors due to mismatches in space and time. SST over a heavily raining area where the data are deficient is interpolated from surrounding nonraining areas.

3. Identification of storm categories

As noted above, the height spectra of precipitating cloud systems have traditionally been investigated based on either radar or infrared measurements. In this section, these measurements are combined to obtain a two-dimensional histogram of PR echo-top height and VIRS brightness temperature. These histograms are presented for the five regions of interest to this study in Fig. 1. Figure 1 shows two noticeable features: a peak in the lower-left corner of many panels and a vertical ridge at 5 km in PR echo-top height. The first peak corresponds to systems with echo-top heights of 2 km and infrared T_b of 280 K, indicating the existence of a distinct group of rainfall trapped in the boundary layer. This group, defined as shallow convection, is the most abundant component of oceanic storms although it makes only a minor contribution to total rainfall. Short and Nakamura (2000) estimated the rain contribution of these systems to be approximately 20% over tropical oceans. Ascribing a physical interpretation to the vertical ridge at an echo-top height of 5 km is more difficult. It is likely an apparent feature rather than a physical entity. As mentioned in section 1, PR echo-top height is sensitive to ice particle characteristics because the PR sensitivity to precipitation ice is marginal and the shape and size of ice particles are highly variable. As a result, inferred echo-top heights are often right

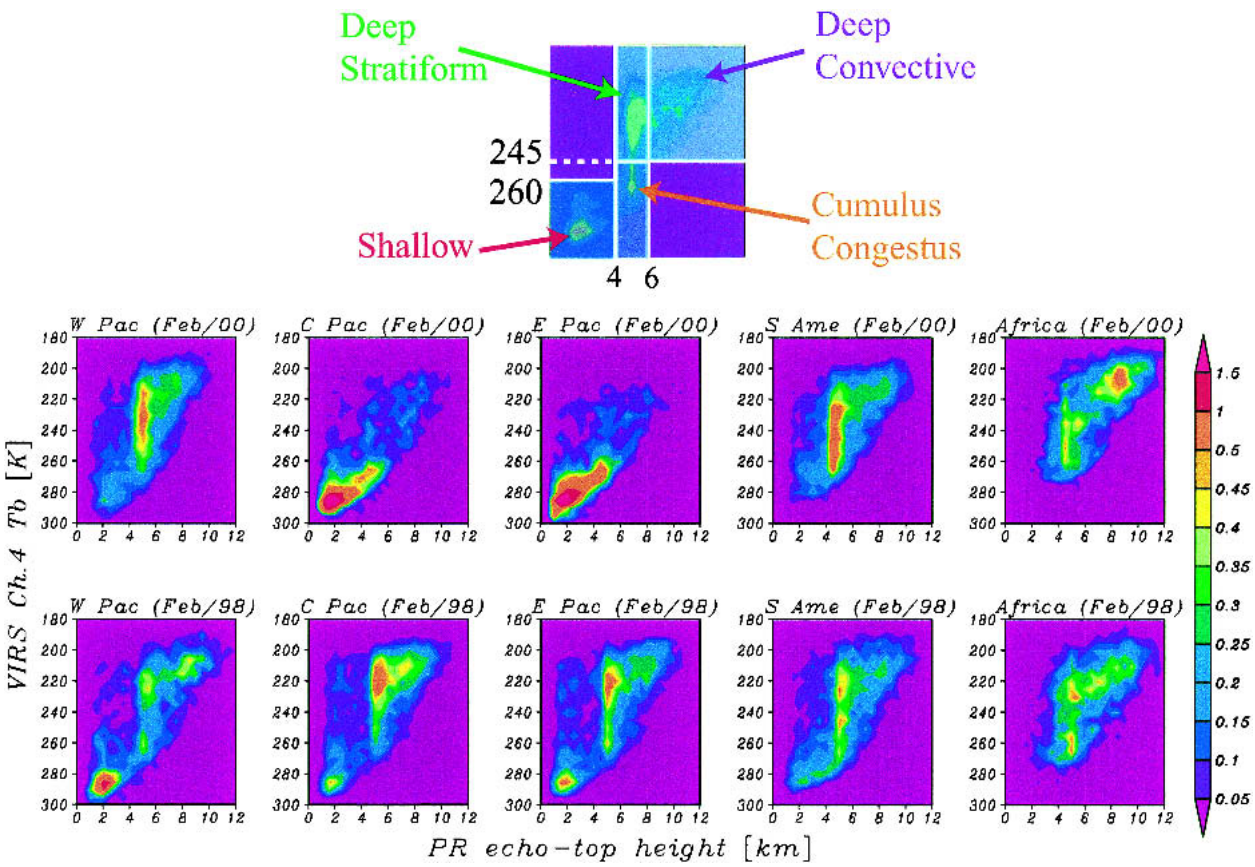

FIG. 1. Two-dimensional histograms of radar echo-top height and infrared brightness temperature along with an illustration showing the storm categories superposed on this diagram. The west Pacific, central Pacific, east Pacific, South America, and Africa are shown, respectively, from left to right for (top) Feb 2000 and (bottom) Feb 1998. The color bar is labeled in the unit of % km^{-1} K^{-1}.The bin size used for mapping the histograms is 0.48 km in PR echo-top height and 4.8 K in infrared T_b, with linear interpolation used for smoothing.

above the melting level, which is 4–5 km in the Tropics, unless the frozen hydrometeors aloft are large enough to be detectable by PR. We infer, therefore, that the observed ridge in the histograms is merely an artifact of the level at which hydrometeors transform from ice to liquid in many storm systems.

It is nevertheless important to note that the range of the freezing-level (FL) ridge in infrared T_b varies between regions and in time. For example, the ridge is well pronounced for 220 K $< T_b <$ 260 K in the west Pacific in 2000, while the central and east Pacific exhibit only a vague remnant of the FL ridge with infrared T_b warmer than 260 K. In most other cases, including the central and east Pacific in 1998, the FL ridge is split into a pair of peaks at 250–260 and 220–230 K. This split may be associated with the presence of cumulus congestus in addition to deep convection. Johnson et al. (1999) found that cumulus congestus clouds, which overshoot the freezing level by 1 to 2 km, consist of a separate component from both shallow cumulus and cumulonimbus in the tropical rainfall spectra. A cloud top at 1–2 km above the freezing height is consistent with the peak at 250–260 K. Machado et al. (1998) discussed the infrared threshold of clouds associated with deep convection and estimated it to be 245 K.

When El Niño is absent (February 2000), the shallow-convection peak is well pronounced in the central and east Pacific, but it is less clear in the west Pacific and completely missing in the continental areas. This trend, consistent with the findings of Short and Nakamura (2000), is understood in terms of the climatological pattern of tropical rainfall. Convection is deepest over the west Pacific warm pool among the three Pacific regions while rainfall is still active along the intertropical convergence zone (ITCZ) but gradually weakens toward the east Pacific. In contrast, the continental regions show a much lower frequency of occurrence of these shallow rain systems. Closer examination, however, reveals that South America shows a weak signature of shallow convection, while Africa does not. This suggests that South American storms form an intermediate type lying somewhere between oceanic rain and highly continental rain, consistent with the "green ocean" (description offered by Williams et al. 2002).

Recent studies have revealed that wet-season convection over the Amazon has two distinct modes called the westerly and easterly regimes (Halverson et al. 2002; Petersen et al. 2002). As a result of local geography, rain systems tend to be more oceanic during the westerly regime and more continental during the easterly regime. These two regimes together would produce a mixture of oceanic and continental rain spectra in monthly statistics seen in Fig. 1.

During El Niño (February 1998), more frequent deep convection takes the place of shallow rain in the central and east Pacific, while the inverse trend is observed in the west Pacific. This pattern is consistent with the eastward shift of heavy precipitation associated with ENSO. Nevertheless, the population of deep convection is still not negligible in the west Pacific in contrast to the central and east Pacific in the normal year. This may be related to the consistently warm SSTs across the Tropics during El Niño as mentioned later in this section. The lack of the noticeable shallow-convection peak, particularly for Africa, makes continental rainfall look more homogeneous over the two periods compared to oceanic regions. This implies that rainfall is dominated more by local conditions over continents than by large-scale circulation. South America, however, exhibits a weak but clear ENSO-related variation, that is, an increase of shallow convection at the expense of deep convection in an El Niño year. This is plausible since ENSO likely has some connection with the synoptic-scale environment that dominates the easterly and westerly regimes in tropical South America. Interestingly, the South American trend is opposite to the central and east Pacific but more like the west Pacific.

The notable change of oceanic storm spectra in response to ENSO may be related to SST. Figures 2 and 3 show the height spectra of storms as presented in Fig. 1, but partitioned by SST, into the three ranges of cool (<26°C), moderate (26°–29°C), and warm (>29°C) SSTs. The histogram is weighted by the frequency of occurrence of SST and is completely blanked for the SST range that never occurred in each region. This SST variability partly accounts for the regional variation in the height spectrum of storms when superposed over the whole range of SST (Fig. 1). For example, the shallow-convection peak is clearly separated from the FL ridge by SST in the west Pacific in 1998, so that the western Pacific spectrum looks more similar to that of the central and east Pacific during El Niño when warm SSTs are isolated. Indeed, the storm spectra are quite coherent across the regions including the west Pacific in 2000 for the warmest range of SST, commonly exhibiting the pronounced FL ridge accompanied with a group of even deeper systems. On the other hand, the storm spectra are less coherent for the lower SST range of 26°–29°C. For these moderate SSTs, the west Pacific in 2000 lacks the shallow-convection peak in contrast to the other Pacific regions in the same year, where shallow convection is overwhelming in number. This zonal gradient in rain spectrum reflects the pattern of the Walker circulation: deep convection is enhanced (suppressed) under continuous large-scale ascent (subsidence). The zonal gradient is somewhat reversed in 1998 for the same SST range, as expected from a change in large-scale circulation associated with ENSO.

Based on Figs. 1, 2, and 3, the observed precipitation events are readily separated into the four storm categories summarized in Table 1. It is noted that the terminology is not precisely parallel to the conventional definitions of shallow convection, cumulus congestus, and the stratiform and convective rains of MCSs. (The storm categories are set in italics throughout the paper to avoid confusion.) In Table 1, the threshold for echo-top height at 4 km (6 km) was chosen as slightly below (above) the FL ridge. The T_b threshold of 260 K is chosen since clouds warmer than this temperature are likely to contain a substantial amount of liquid cloud water including supercooled droplets. A colder threshold of 245 K was chosen to partition the FL ridge following Machado et al. (1998). It was found that changing this value by 5° did not to have any qualitative impact on the results discussed below. There are two regimes that do not belong to any of the four categories; echo tops higher than 6 km with T_b warmer than 245 K and echo tops lower than 4 km with T_b colder than 260 K, both of which make only negligible contributions to the total population of storms. The former case is physically implausible since radar echo-top heights are unlikely to exceed cloud-top heights. The latter case corresponds to shallow rain overlapped with separate high- or middle-level clouds.

A major component of the first category is the shallow-convection peak, and hence this category is designated by *Shallow*. The warm-rain process dominates rainfall production in this category because cloud top is not high enough to be capable of producing an appreciable number of frozen particles. The *Cumulus congestus* category contains rainfall that develops beyond the freezing height by a kilometer or two, but convection is not deep enough to reach the tropopause. The third category, denoted as *Deep stratiform*, consists of events that have very cold cloud tops while their echo-top heights remain at the freezing level. *Deep convective* events, which constitute the final category, have cloud tops as cold as *Deep stratiform* events but have echo-top heights developing far beyond the freezing level. The *Deep stratiform* and *Deep convective* categories, separated by a difference in their capability to create large ice hydrometeors, were named based on the common understanding of the MCS structure (e.g., Fig. 9.34 of Houze 1993); large ice particles formed in the convective region, which would create detectable radar echoes much above the freezing level, are advected through the upper troposphere to the stratiform region where they precipitate in the absence of sustained vertical updrafts. As a consequence, rainfall near or within the deep convective cores would be categorized as

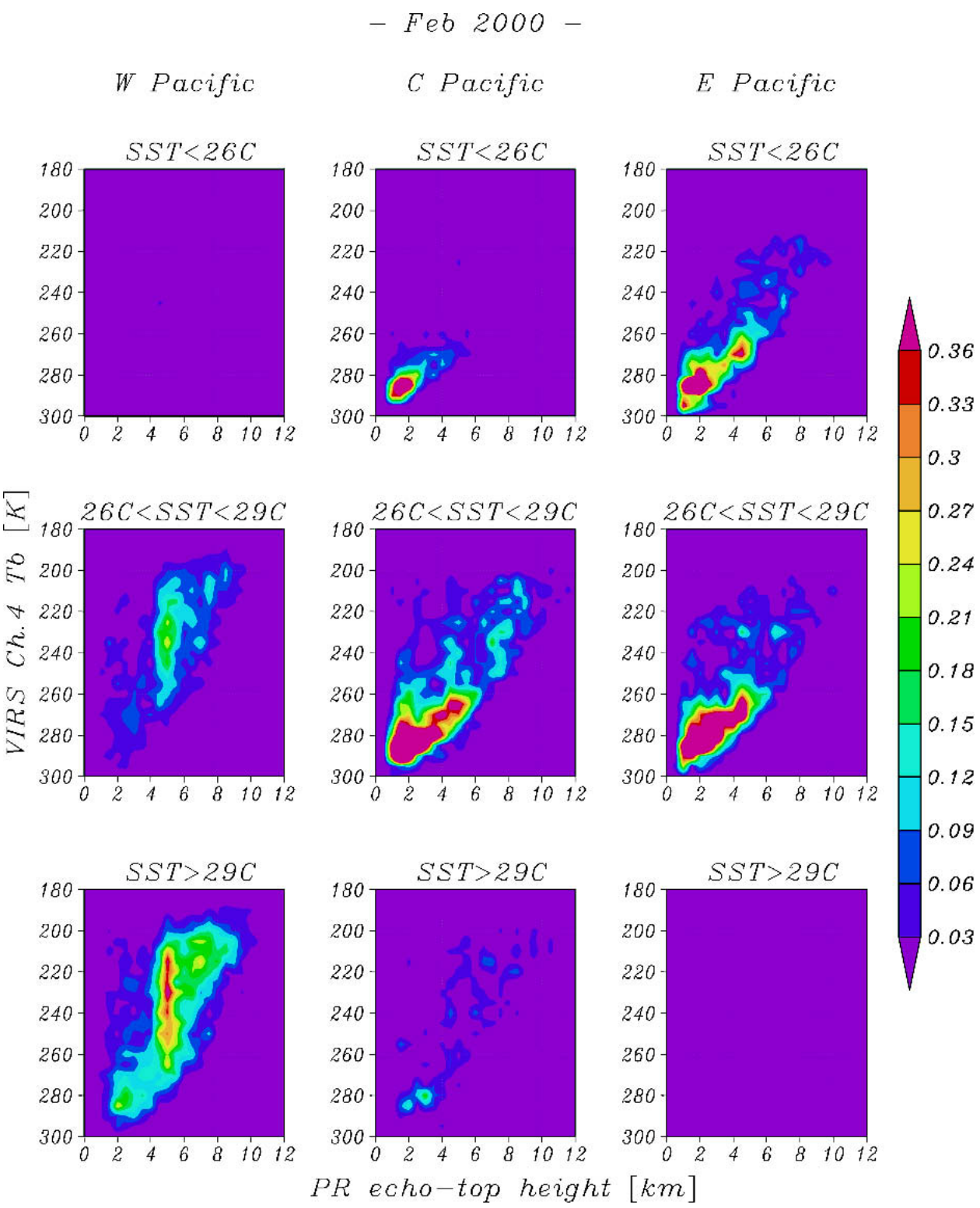

FIG. 2. Same as in Fig. 1, but partitioned by SST. Histograms of cool SSTs (<26°C), moderate SSTs (26°–29°C), and warm SSTs (>29°C) are shown, respectively, from top to bottom: for the (left) west, (middle) central, and (right) east Pacific. The time period is Feb 2000. The color bar is labeled in the unit of % km^{-1} K^{-1}.

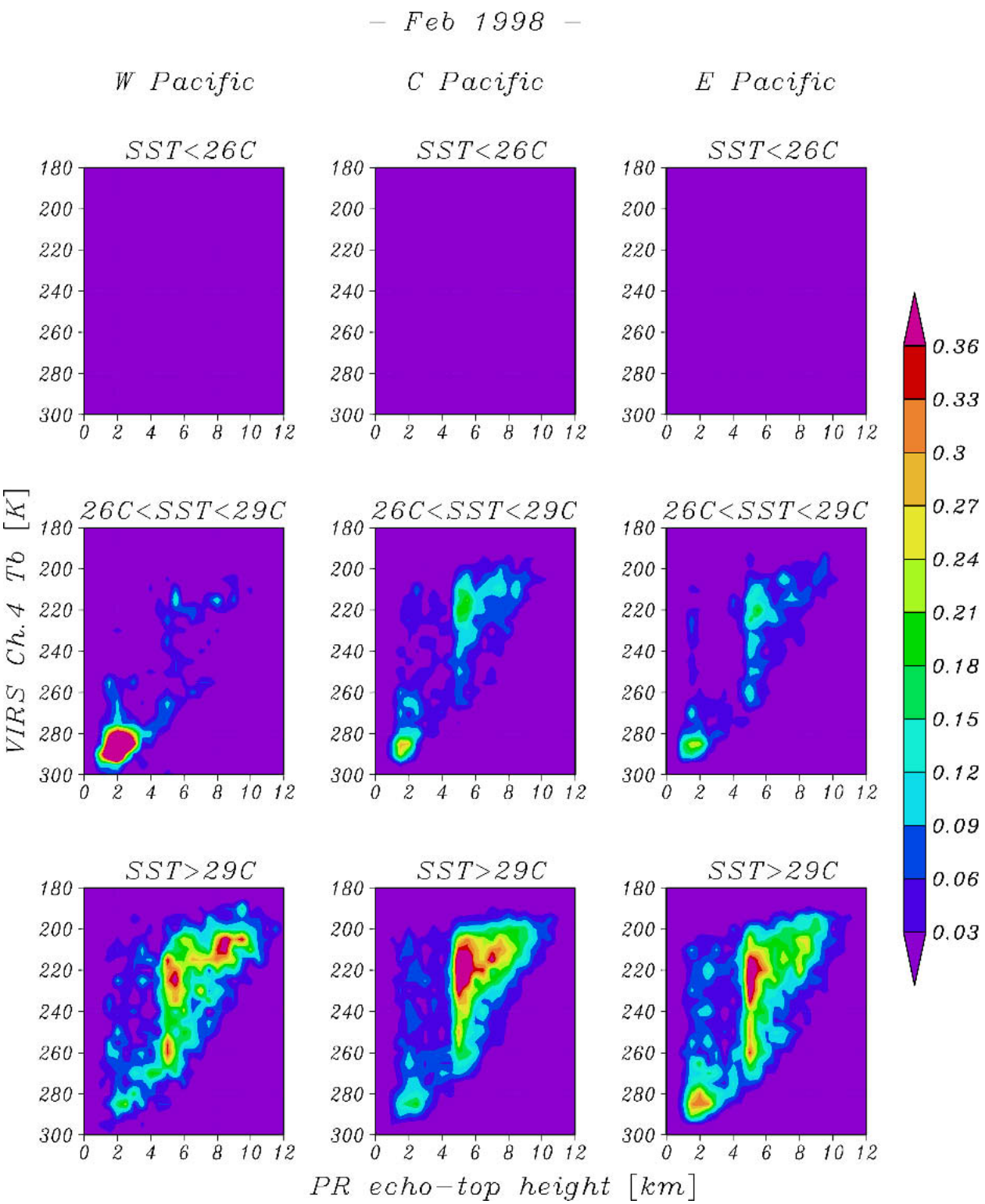

FIG. 3. Same as in Fig. 2, but for Feb 1998.

TABLE 1. Definition of storm categories.

Storm category	Radar echo-top height	Infrared T_b
Shallow	<4 km	>260 K
Cumulus congestus	4–6 km	>245 K
Deep stratiform	4–6 km	<245 K
Deep convective	>6 km	<245 K

Deep convective systems, and *Deep stratiform* events take their place farther away from the convective cores. It is important to note that *Deep convective* events may contain a considerable amount of "stratiform" rain in the vicinity of deep convective cores where large frozen particles can be as abundant as in the convective regions. The statistical relation between the storm categories and the traditional stratiform/convective classes is examined in section 5.

Figures 4 and 5 show rain probability or raining area fraction as a function of SST for each storm category identified above. The histogram of SST is given as well to demonstrate the relative frequency of SST occurrence. The histograms imply that 1) in a normal year (Fig. 4), the west Pacific exhibits a peak as high as 29°–30°C, while the maximum SST probability decreases to around 25°C for the central and east Pacific, and 2) SST is consistently warmer than 25°–26°C over the entire tropical Pacific during the 1997–98 El Niño event (Fig. 5). The absence of warm or cold SSTs in some cases accounts for blank panels in Figs. 2 and 3; for example, SST < 26°C in 1998.

The dependence of rain probability on SST varies with regions and years. There is nevertheless a general trend that *Shallow* events have the highest probability of occurrence for relatively cold SSTs, while *Deep convective* events take their place for warmer SSTs. The turnover occurs at 28° or 29°C for all the regions and years except the west Pacific in 2000, where deep systems dominate for the entire range of SST. Once SST exceeds this threshold, the probability of occurrence of *Deep convective* systems shows a rapid increase with SST, while *Shallow* and *Cumulus congestus* events generally exhibit only a weak dependence on SST above the threshold. The value of 28°–29°C is therefore a re-

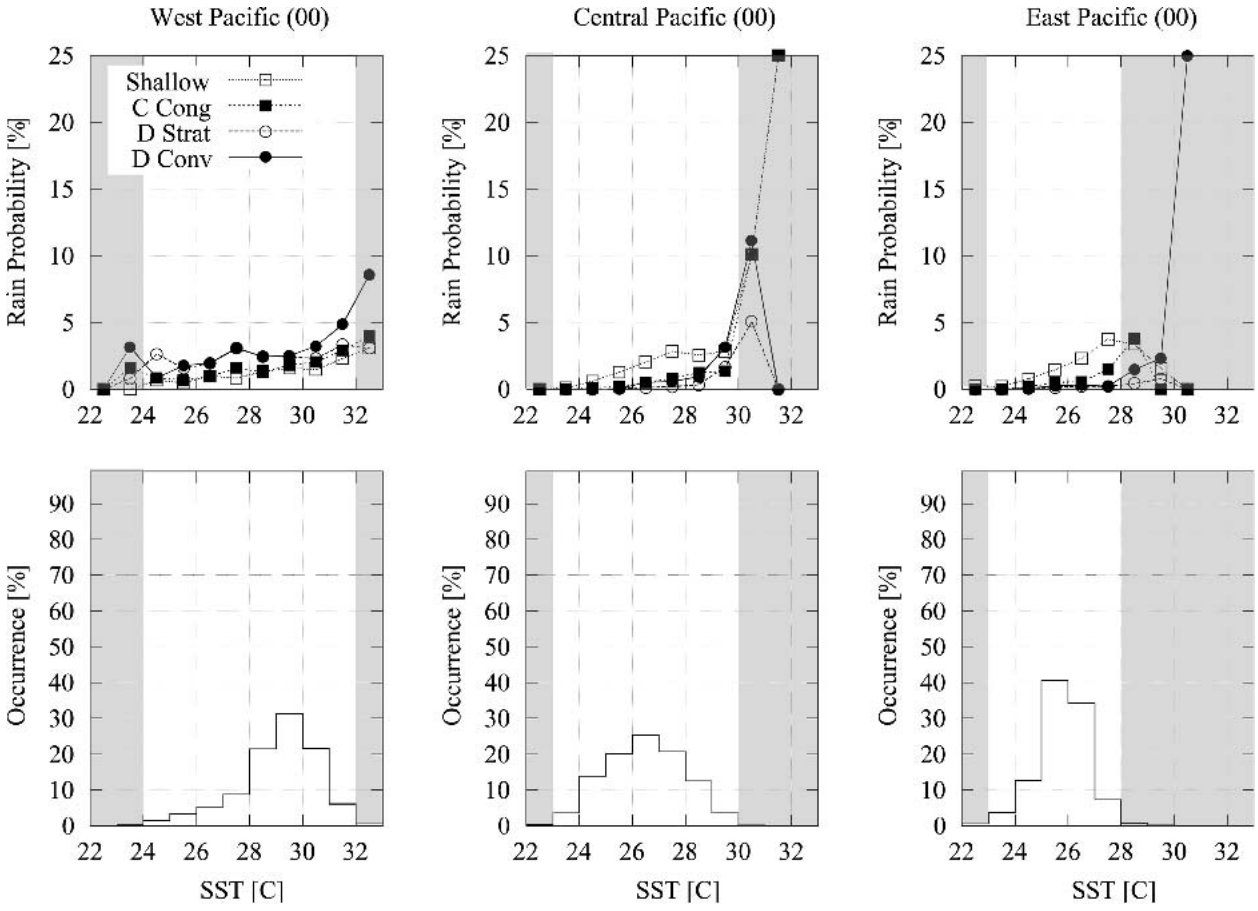

FIG. 4. (top) Rain probability, or raining area fraction, as a function of SST for each storm category over the (left) west, (middle) central, and (right) east Pacific in Feb 2000. (bottom) The histogram of SST for all raining and nonraining pixels. The SST range corresponding to a less than 1% chance of occurrence is shaded.

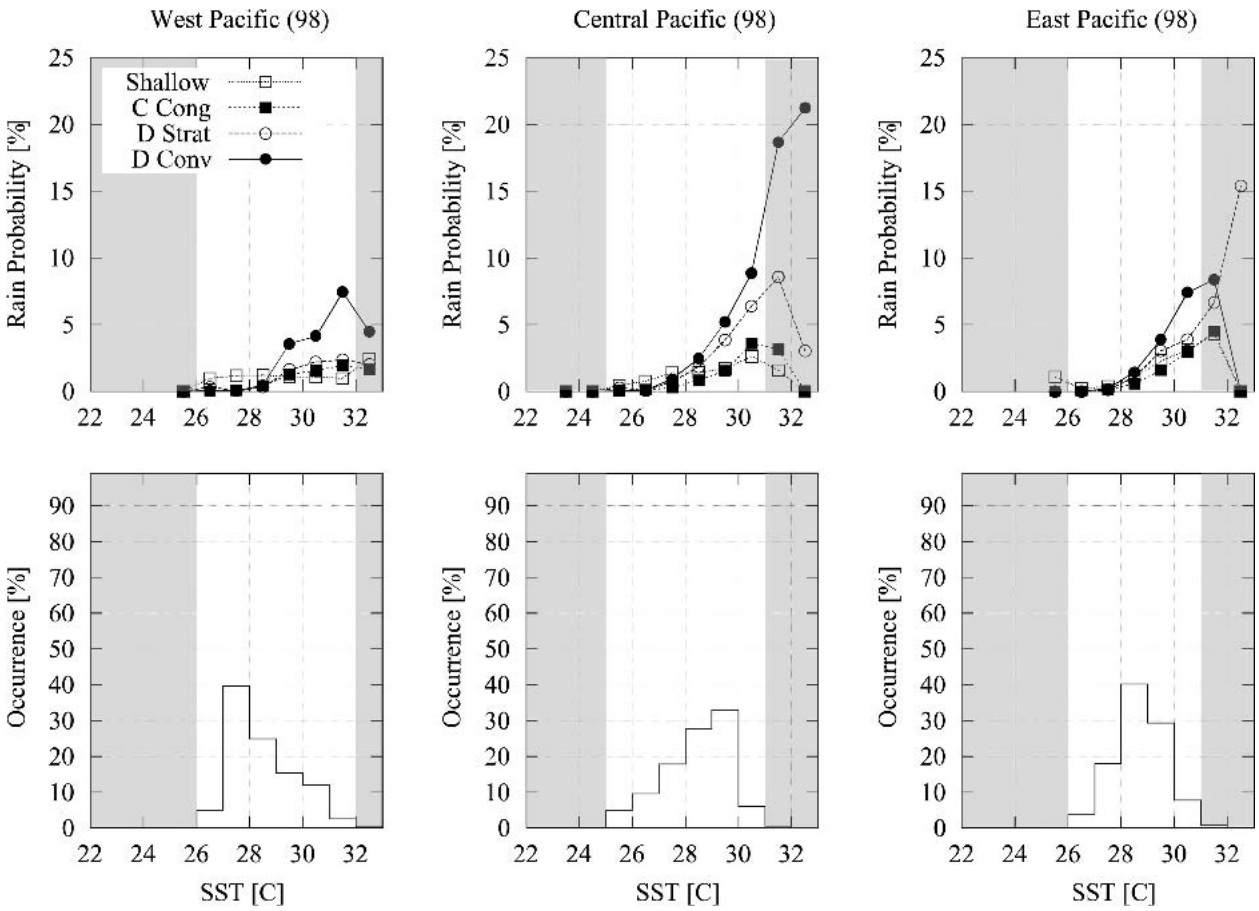

FIG. 5. Same as in Fig. 4, but for Feb 1998.

gime-independent SST threshold beyond which deep systems generally prevail, with the exception of the western Pacific warm pool in a normal year where deep systems dominate for all SST. This accounts for the coherent spectral pattern for warm SSTs that we have seen in Figs. 2 and 3.

Figures 4 and 5 indicate that rain probability tends to decrease near the high end of SST range except in the west Pacific in 2000. It is, however, not clear that this trend is real because such high SSTs are so rare that its statistical significance is not necessarily assured (the SST range that corresponds to a less than 1% chance of occurrence is shaded in the figures). A more extensive study using a larger dataset is necessary to discuss the physical mechanism behind the interaction between precipitation and environmental factors such as SST.

4. Correlation-scale length of storms

a. Theory and case study

The categorization described in section 3 is based solely on the vertical extent of storms. It is also important to develop a framework for investigating their horizontal properties to allow us to draw a three-dimensional picture of various tropical storms. The CSL is introduced for this purpose, and its mathematical basis is provided in this section. Together with the classification system developed in section 3, the CSL will be used to analyze the character of precipitation systems inferred from satellite data later in this section.

First, we introduce the fractional coverage of raining scenes, at a distance d from a reference point x_{ref},

$$f_r(d_i, x_{\mathrm{ref}}) = \frac{n_r(d_i)}{n_{\mathrm{tot}}(d_i)}, \tag{1}$$

where n_r is the number of raining PR pixels and n_{tot} is the total number of PR pixels within a distance bin defined around $d = d_i$. Similarly, the fractional coverage of cloudy scenes is given as

$$f_c(d_i, x_{\mathrm{ref}}) = \frac{n_c(d_i)}{n_{\mathrm{tot}}(d_i)}, \tag{2}$$

which is (conceptually) the number ratio of cloudy VIRS pixels n_c to the total VIRS pixels. Cloudiness is, however, difficult to define uniquely from infrared radiances, and hence we introduce the average brightness temperature within a distance bin around $d = d_i$,

$$\overline{T}_b(d_i, x_{\text{ref}}) = \frac{\sum T_b(d_i)}{n_{\text{tot}}(d_i)}, \quad (3)$$

as a proxy of f_c based on the relationship between $\overline{T}_b$ and f_c described as follows. The summation of T_b in (3) may be interpreted as a combination of the cloud-top temperature, T_c, and ambient field (sea surface and/or extended low clouds) temperature, T_a, that is,

$$\sum T_b(d_i) \approx T_c n_c(d_i) + T_a[n_{\text{tot}}(d_i) - n_c(d_i)]. \quad (4)$$

The equality in (4) is exact if clouds consist of optically thick high clouds with a homogeneous top height and ambient low clouds (or no low clouds). Combining (3) and (4), one gets

$$\overline{T}_b(d_i, x_{\text{ref}}) = (T_c - T_a) f_c(d_i) + T_a, \quad (5)$$

which claims that $\overline{T}_b(d_i, x_{\text{ref}})$ is linearly related to $f_c(d_i)$.

Figure 6 shows a snapshot of an MCS observed by TRMM, demonstrating examples of f_r (d, x_{ref}) and $\overline{T}_b(d, x_{\text{ref}})$ for four reference points that belong to different storm categories. In Fig. 6, the satellite swath split into three slips is illustrated to show infrared T_b, PR echo-top height, and the storm categories. An MCS is outlined by very cold T_b (blue and purple regions in the bottom slip), including deep convective cores punctuated by PR echo-top heights as high as 10 km (purple in the middle slip) and stratiform regions having relatively lower echo-top heights. The storm categories shown in the top slip clearly separate the MCS traced by *Deep stratiform* (blue) or *Deep convective* (purple) from the sparsely distributed components of *Cumulus congestus* (green) and *Shallow* (red).

Figure 6 also shows f_r (d, x_{ref}) and $\overline{T}_b(d, x_{\text{ref}})$ computed for each of the four reference points, around

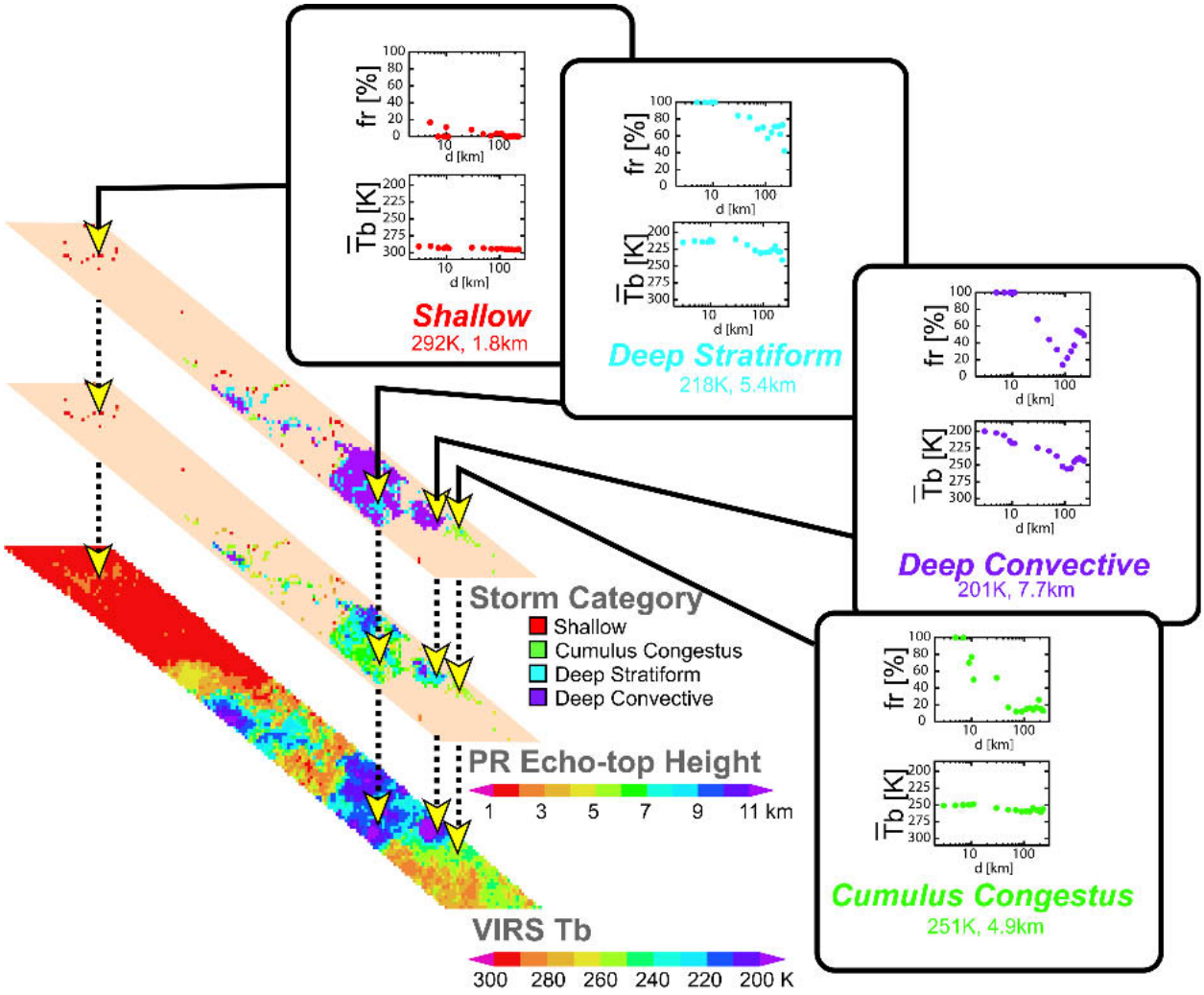

FIG. 6. A snapshot of an observed MCS by TRMM, showing (bottom slip) infrared T_b, (middle slip) radar echo-top height, and (top slip) storm categories, together with $f_r(d)$ and $\overline{T}_b(d)$ computed around each of four sample points belonging to different storm categories. The positions of the sample points on the satellite swath are designated by arrows. A pair of numbers provided for each sample points (i.e., 292 K, 1.8 km) indicates infrared T_b and radar echo-top height, respectively, at that point.

which (1) and (3) were performed over nearby satellite pixels. For example, f_r around the *Deep stratiform* event remains as high as 60% (and $\overline{T}_b$ as cold as 230 K) even for $d > 100$ km, indicating that this event is surrounded by a very extensive high cloud with precipitation over 60% of it in areal coverage.[1] One can see that the *Deep convective* and *Deep stratiform* events exhibit a turnover at $d = 100$ km in f_r and $\overline{T}_b$, detecting the adjacent raining cells. As such, f_r and $\overline{T}_b$ are sensitive to neighboring cells and therefore reflect the horizontal extent of an entire organized system regardless of the contiguity of raining areas. A distinctive cluster of *Cumulus congestus* can be seen right next to the MCS, showing a rapid decay in f_r and a nearly constant $\overline{T}_b$. This implies that *Cumulus congestus* systems are constituted of isolated rainfall associated with extended clouds, most of which are nonprecipitating. A similar trend is found even more clearly for the *Shallow* event, which is so isolated and sparse that f_r reaches zero at 100 km away from the reference point.

Before proceeding, some thought experiments are applied to provide insight into the physical meaning of the CSL. Figures 7a–d schematically demonstrate the relations between f_r and storm size including the cases with storms truncated by the swath edges. In every case, D_i (i = a–d) is given as a reference dimension characteristic of each graph of $f_r(d)$. The simplest case, a_1, illustrates an isolated convective cell with a reference point nearly at its center, where D_{a1} provides a reasonable approximation of the cell radius. For another reference point closer to the edge of the same convective cell (case a_2), f_r is expected to decrease with increasing d more rapidly near $d = 0$ but have a longer "tail" at a large d since the cell is measured across from one edge to the other, and thus D_{a2} is closer to the diameter than to the radius. In case b, representative of an extensive and more or less circular system, D_b is still close to the actual storm size despite the fact that the storm is so large that it is truncated by the satellite swath. A heavily elongated storm such as the "MCS linear" system described by Rickenbach and Rutledge (1998) can be measured along either its short or long axis, D_{c1} or D_{c2} in cases c_1 and c_2, depending on the storm orientation. If a significant fraction of the storm lies outside the swath as shown in case d, D_d could be smaller than the actual size of a storm. A parallel discussion applies to $\overline{T}_b$ by replacing f_r with f_c.

Although D_i in an individual case is not always a satisfying representative of storm size, it is possible to extract a more robust and objective estimation by examining the statistics of a large number of observations. The expectation of finding rain, $\langle f_r \rangle$, at a distance d from a given raining point is therefore introduced as

$$\langle f_r \rangle(d) = \frac{1}{A_r} \int_{A_r} f_r(d, x_{\text{ref}}) \mathrm{d}x_{\text{ref}}, \tag{6}$$

where f_r (d, x_{ref}) is integrated over reference points across the raining area of interest, A_r. In the actual analysis of finite datasets, (6) is rewritten as

[1] In this context, "f_r (or $\overline{T}_b$) around a *Deep convective* event" means "f_r (or $\overline{T}_b$) of any kind of rainfall (or clouds) surrounding a *Deep convective* event" and should not be considered as "f_r ($\overline{T}_b$) deduced exclusively from the raining (cloudy) pixels classified into *Deep convective* systems." The former definition is crucial for addressing problems such as a variation in the horizontal extent of cirrus anvils associated with a certain type of storms, which is a major interest of this study.

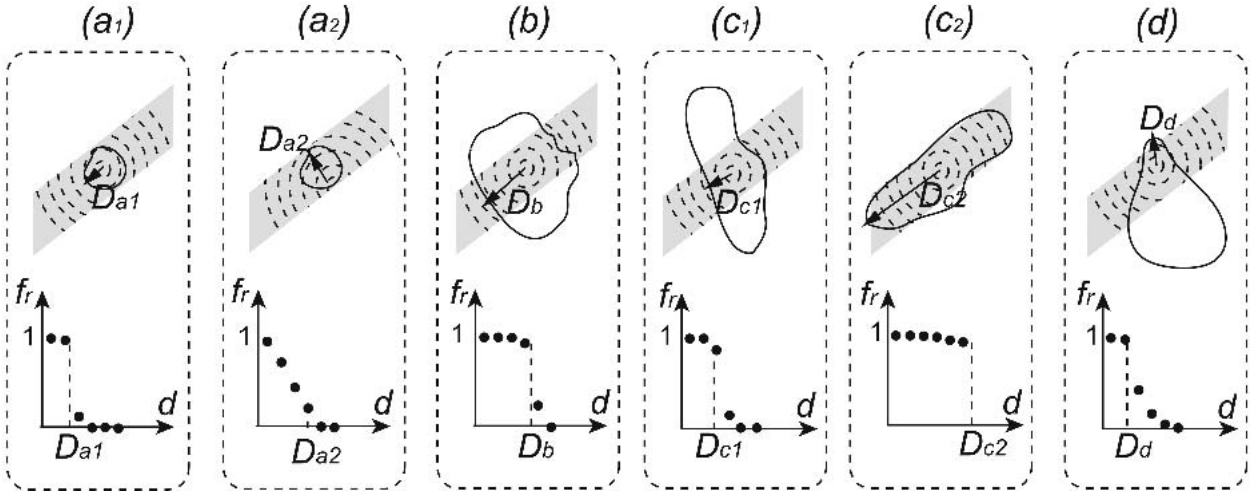

FIG. 7. Schematic illustrations of $f_r(d_i, x_{\text{ref}})$ for several examples, where d_i is the distance of the ith circular bin (dashed circles) from a given reference point (the center of the innermost bin), x_{ref}. In each case, an example of an observed rainfall system and the overlaid satellite swath (shaded) are illustrated together with the expected form of $f_r(d_i, x_{\text{ref}})$, where each plot represents the raining-area coverage within a circular bin, and D_i denotes a reference dimension. See text for more details.

$$\langle f_r\rangle(d_i)=\frac{1}{N_{\rm ref}}\sum^{N_{\rm ref}} f_r(d_i, x_{\rm ref}), \tag{7}$$

where $N_{\rm ref}$ is the total number of reference points. Similarly, the expectation of $\overline{T}_b(d, x_{\rm ref})$, $\langle T_b\rangle$, is defined as

$$\langle T_b\rangle(d) = \frac{1}{A_r}\int_{A_r} \overline{T}_b(d, x_{\rm ref})dx_{\rm ref} \approx \frac{1}{N_{\rm ref}}\sum^{N_{\rm ref}} \overline{T}_b(d_i, x_{\rm ref}). \tag{8}$$

In the averaging process, f_r with different reference points for the same storm system such as in cases a_1 and a_2 would result in a smoothly decaying function for $\langle f_r\rangle$ with a decaying rate indicative of the storm size, likely somewhere between its radius and diameter. Similarly, the extreme cases as shown in c_1 and c_2 of Fig. 7 tend to statistically cancel each other out, leaving a moderate value between D_{c1} and D_{c2}, if the storm orientation with respect to the flying direction of the satellite should be randomly distributed. Furthermore, the underestimation of storm size as seen in case d does not considerably affect $\langle f_r\rangle$ as long as the number of observations is sufficient to dilute statistically rare events such as case d. As a result, $\langle f_r\rangle$ is far less sensitive to the truncation effect compared to the contiguous pixel method, which would underestimate the size of storms for 17% of total rain systems and 82% of MCSs in the use of TRMM PR (Nesbitt et al. 2000).

Computing (1) and (7) across a given geographical region and time period, one obtains $\langle f_r\rangle$ and its standard deviation, σ_r, as functions of d_i. The resultant $\langle f_r\rangle$ is expected to decrease monotonically with increasing d because storm size spectra are known to be decreasing functions in general (López 1976, 1977; Machado et al. 1992; Machado and Rossow 1993; Del Genio and Kovari 2002). An exponential function is adopted to fit the data for extracting a characteristic scale length from $\langle f_r\rangle$ as a function of d. The RCSL, λ_r, is thus defined by minimizing

$$\sum_i \left[\frac{\ln\langle f_r\rangle(d_i) - \ln F_{r0} + d_i/\lambda_r}{\sigma_r(d_i)}\right]^2 \tag{9}$$

to find the least square fit to the data using an exponential form,

$$\langle f_r\rangle(d) \sim F_{r0}\exp(-d/\lambda_r). \tag{10}$$

The fitting function for the cloud CSL (CCSL), λ_c, is similarly defined from (5) as

$$\langle T_b\rangle(d) \sim (T_c - T_a)\exp(-d/\lambda_c) + T_a, \tag{11}$$

where T_c and λ_c are determined under a given T_a. The ambient field temperature T_a is determined from infrared observations as described in the next subsection.

b. Results

The RCSL and CCSL introduced above are now applied to satellite data and sorted by the storm categories defined in section 3. The procedure of the analysis can be seen in Fig. 8, which illustrates $\langle f_r\rangle$ and $\langle T_b\rangle$ along with fitted exponential curves as a function of d. While only western Pacific storms in February 2000 are shown, the results for all other cases are qualitatively similar. Figure 8 should not be confused with the probability distribution constructed by the contiguous pixel method, where a storm size is defined individually for each separate system, as often found in the literature. The definitions of $\langle f_r\rangle$ and $\langle T_b\rangle$ are based on the spatial structure of the rain/cloud fraction without explicitly identifying "size" for individual storms (see the previous subsection for details).

For rain systems around *Shallow* events, $\langle f_r\rangle$ shows a rapid decrease for $d < 10$ km until it reaches a constant value at $\langle f_r\rangle = 10\%$ on a larger scale. As demonstrated in Fig. 6, this implies that unorganized convective cells whose horizontal scales do not exceed 10 km are typically observed around *Shallow* events. The flat component in $\langle f_r\rangle$ ($d > 30$ km) has been excluded from the exponential fit because it only reflects the ambient field of sparsely distributed cumulus clouds that do not consist of a single organized system. Infrared brightness temperature is found to be independent of d for the *Shallow* category over all scales of interest. This feature, together with the trend in $\langle f_r\rangle$, indicates that *Shallow* events are embedded in an extended ambient field, 90% of which consists of nonprecipitating clouds and/or clear sky. For the *Shallow* category, therefore, $\langle T_b\rangle$ is fitted by a straight horizontal line instead of an exponential curve. This horizontal line defines T_a in (4), which reads $T_a = 275$ K in this particular case. The ambient field temperature defined in this way for each geographical region is adopted to determine the CCSL around *Deep stratiform* and *Deep convective* systems according to (11). Such low, extensive clouds as those that contribute to T_a are expected to cool the planet by reflecting more solar radiation to space than can be compensated for by latent heat released in their formation.

In contrast to *Shallow* events, both $\langle f_r\rangle$ and $\langle T_b\rangle$ exhibit an extensive structure over the whole range of d around *Deep convective* systems, indicating that they are generally organized on a scale of hundreds of kilometers. A plateau is observed in the inner portion of $\langle T_b\rangle$ while $\langle f_r\rangle$ drops more quickly as d increases, indicative of a raining core associated with a more extended high cloud such as anvil cirrus. Precipitating cores in those storms release a significant amount of latent heat, likely overwhelming the infrared heating and the shortwave cooling by the associated clouds.

The general properties of *Cumulus congestus* events (not shown) resemble those of *Shallow* events, while *Deep stratiform* systems are more similar to *Deep con-*

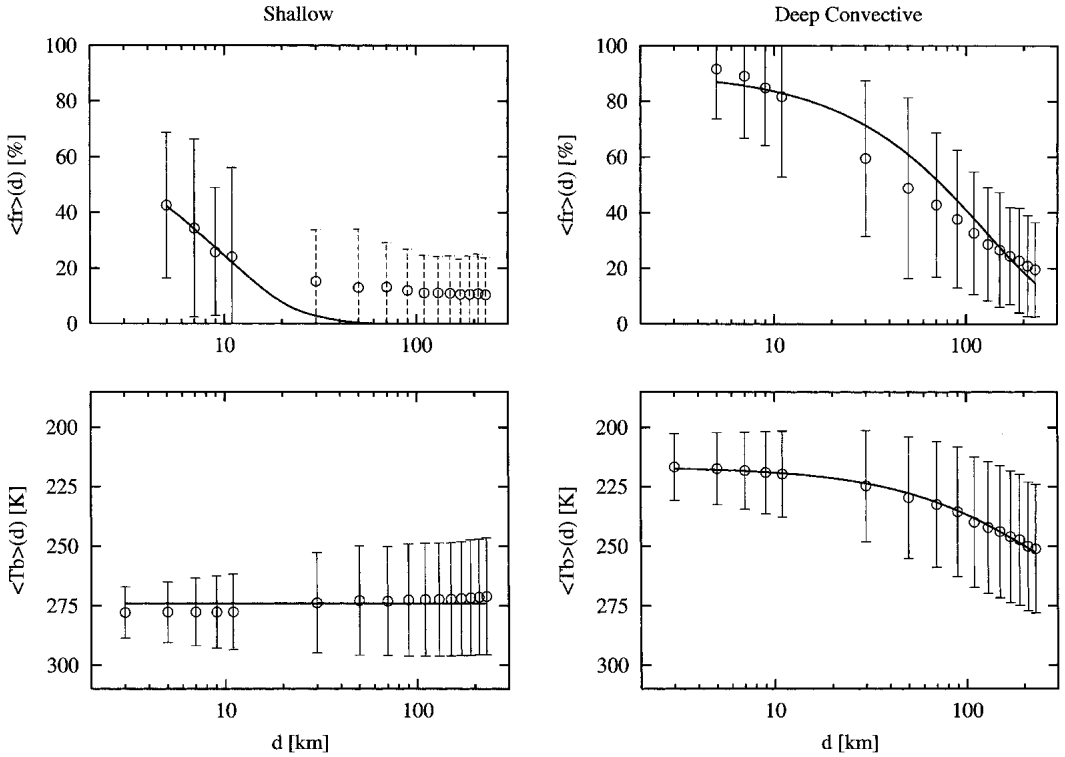

FIG. 8. (top) Here $\langle f_r \rangle$ and (bottom) $\langle T_b \rangle$ are shown as functions of distance for the (left) *Shallow* and (right) *Deep convective* categories. All cases exhibit qualitatively similar patterns to this particular case of the west Pacific in Feb 2000. Open circles, error bars, and solid curves show the average, standard deviation, and fitted exponential function, respectively.

vective ones. The CCSL is not well defined around the *Shallow* and *Cumulus congestus* categories because the major cloud component consists of extensive nonprecipitating clouds that are not associated with the storm. The CCSL is therefore evaluated only for the clouds surrounding *Deep stratiform* and *Deep convective* events. The RCSL is estimated only from the inner portion of data ($d < 10$ km) around *Shallow* and *Cumulus congestus* events, whereas it is derived from the entire range of d when calculated around *Deep stratiform* and *Deep convective* systems. Note that the RCSL and CCSL can exceed the largest d used for the exponential fit when $\langle f_r \rangle$ and $\langle T_b \rangle$ decay very slowly with d.

Table 2 summarizes estimated values of RCSL and CCSL for February 1998 and 2000. The RCSL ranges from 8 to 13 km for *Shallow* events and from 13 to 18 km for *Cumulus congestus* systems over the five regions studied. No notable regional and ENSO-related vari-

TABLE 2. RCSL and CCSL. The CCSL is not defined for *Shallow* and *Cumulus congestus* categories. The results correspond to the months of Feb 2000 and Feb 1998 (in parentheses).

	West Pacific	Central Pacific	East Pacific	South America	Africa
RCSL (km)					
Shallow	9.25	9.33	9.50	12.6	12.3
	(7.82)	(9.16)	(12.4)	(11.8)	(12.9)
Cumulus congestus	13.0	15.9	14.7	16.1	14.9
	(14.0)	(16.6)	(17.8)	(15.8)	(14.6)
Deep stratiform	153	137	111	165	144
	(156)	(221)	(189)	(142)	(120)
Deep convective	126	124	103	120	119
	(136)	(170)	(151)	(122)	(101)
CCSL (km)					
Deep stratiform	324	220	180	278	293
	(365)	(498)	(382)	(309)	(270)
Deep convective	233	188	134	173	215
	(270)	(317)	(250)	(231)	(178)

ability is found in RCSL for these storms. On the other hand, *Deep stratiform* and *Deep convective* events are accompanied with RCSL and CCSL consistently larger than 100 km. The RCSL and CCSL around *Deep stratiform* and *Deep convective* systems over ocean exhibit a significant increase during the 1998 El Niño event compared to the year 2000, and the increase is most conspicuous for the central and east Pacific. Furthermore, while western Pacific convection is generally not as deep in El Niño years, the RCSL and CCSL increase slightly during the 1998 El Niño event in the west Pacific.

Figure 9 illustrates the relationship between CCSL and RCSL for *Deep stratiform* and *Deep convective* events for both February in 1998 and 2000. As expected, the CCSL is always larger than the RCSL because anvil cirrus detrained from deep convection can extend horizontally far beyond the raining area. Two other noticeable but less expected features are also found in Fig. 9. First, all plots are more aligned than scattered in Fig. 9, independent of storm categories and geographical regions. Second, both the RCSL and CCSL are always larger around *Deep stratiform* events than *Deep convective* events. The excess of *Deep stratiform* CCSL over *Deep convective* CCSL is most outstanding for the central and east Pacific in 1998, where the former is more than 1.5 times larger than the latter. The temporal change in the stratiform/convective ratio through an MCS life cycle discussed in the next section helps explain some of these behaviors.

5. Discussions

This section is dedicated to discussing our results in the context of those presented in related prior studies. We start with an attempt to relate the present storm categorization with common classifications of tropical storms.

a. Comparison to convective/stratiform rain types

Although the present storm categorization is by no means intended to replace the conventional stratiform/convective classification, these two different categorizations are briefly compared in this subsection. The stratiform (convective) area fraction, as defined by the number of PR stratiform (convective) pixels divided by the total raining pixels, is summarized in Table 3 for each storm category as well as the mean, integrated over all the categories. With no qualitative difference between the two years, the *Shallow* and *Deep stratiform* categories exhibit the highest stratiform fractions. In contrast, *Cumulus congestus* and *Deep convective* categories contain larger fractions of convective rain area than its mean value.[2] *Deep convective* events are made up of twice as much convective rainfall as *Deep stratiform* events, as expected from the nomenclature. At the same time, however, *Deep convective* events include a significant fraction of stratiform rain. As pointed out in section 3, *Deep convective* systems contain the stratiform regions of MCSs in the neighborhood of deep convective cores where large ice particles created in the convective cores directly flow in.

The difference in the stratiform/convective ratio could account for the difference in RCSL and CCSL

[2] The high stratiform ratio for *Shallow* events should be interpreted with care because Schumacher and Houze (2003) pointed out that shallow, isolated rain is classified as stratiform in the 2A23 dataset in spite of its convective nature.

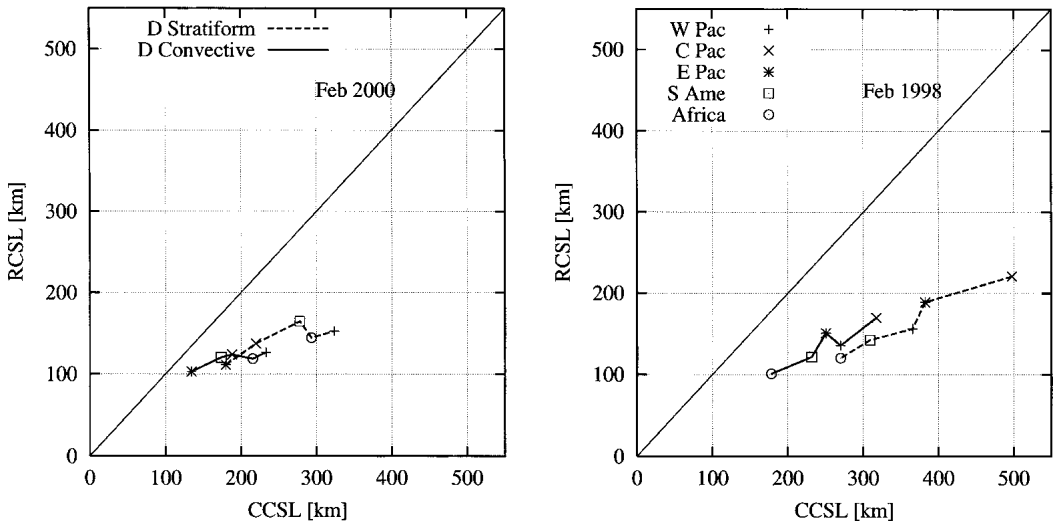

FIG. 9. RCSL vs CCSL for *Deep stratiform* and *Deep convective* events. Lines and symbols are designated in the figure.

TABLE 3. Stratiform/convective percentage relative to total rainfall for each storm category with the mean ratio integrated over all the categories. The residual percentage unlisted here is classified as "others" in the TRMM operational rain classification (2A23) dataset.

	Stratiform		Convective	
	2000	1998	2000	1998
Shallow	83%	85%	14%	12%
Cumulus congestus	74%	73%	21%	21%
Deep stratiform	83%	86%	11%	9%
Deep convective	60%	70%	22%	17%
Mean	74%	77%	17%	14%

between the *Deep convective* and *Deep stratiform* categories in the context of the MCS life cycle. Individual convective cells grow and merge in the developing stage of the life cycle of an MCS (Fig. 10a), but it is not until the mature stage that an extensive stratiform region develops (Fig. 10b). Convective elements weaken during the decaying stage of the life cycle, leaving behind stratiform precipitation (Fig. 10c; see also chapter 9.1.3 of Houze 1993). The developing stage would therefore produce *Deep convective* profiles with a relatively small CSL, and the extensive stratiform component would contribute to a large CSL around *Deep stratiform* events through the mature and dissipating stages. Integrated over the entire life cycle of MCS, *Deep stratiform* systems would therefore be accompanied with a larger CSL than *Deep convective* events.

Takayabu (2002) demonstrated that rain intensity monotonically increases as rain tops become higher, with the exception of stratiform rain with the rain-top height exceeding 8–9 km. She also found that convective rain has a higher rain rate than stratiform rain for a given rain-top height. The high echo-top heights together with the high convective ratio, therefore, allow *Deep convective* events to produce the most intense rainfall over the Tropics.

b. Alternate classifications

Rickenbach and Rutledge (1998) defined four rainfall classes based on the horizontal scale and morphology of radar-echo distributions: sub-MCS nonlinear, sub-MCS linear, MCS nonlinear, and MCS linear. They investigated rainfall/number distributions of convective feature height separately for each of the four classes. They found that MCS linear events are associated with deep convection, while sub-MCS nonlinear events exhibit a distinct frequency peak at 3–4 km in vertical profiles. A similar relationship between the vertical extent and horizontal organization was found in section 4. The RCSL around *Shallow* and *Cumulus congestus* events indicates that they represent no more than

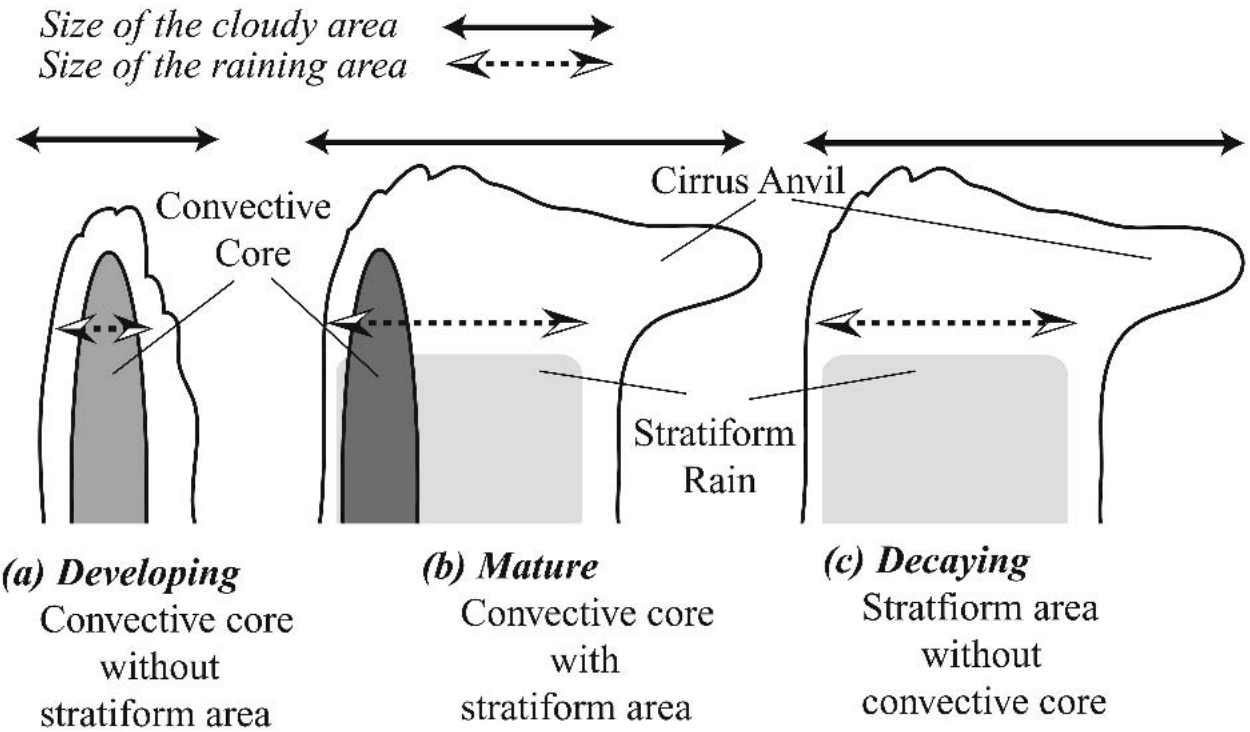

FIG. 10. Schematic diagram illustrating the life cycle of an MCS. *Deep convective* systems, sensitive to convective cores, are observed at the (a), (b) earlier stages of an MCS life cycle, while *Deep stratiform* events, more sensitive to stratiform rain, take the place at the (b), (c) later stages. Accordingly, the RCSL and CCSL are expected to be smaller for *Deep convective* systems than for *Deep stratiform* systems when integrated over the life cycle.

small-scale isolated convection, while the CSL associated with *Deep stratiform* and the *Deep convective* represents organized systems as large as an MCS scale.

Size distributions of cloud clusters have also been studied using infrared brightness temperatures acquired by geostationary satellites. The mean size of cloud clusters ranges from 50 to 300 km in terms of the equivalent radius (or radius of a circle having the same area) as estimated from contiguous cloud areas colder than a certain threshold (e.g., Machado et al. 1992; Chen et al. 1996). The CCSL obtained in the present study is at the high end of the largest clusters found in past work. This is reasonable since the CSL is more sensitive to the size of a whole system rather than that of an individual element identified as a contiguous area.

More recently, the contiguous pixel method was applied directly to rainfall based on microwave scattering signals at 85 GHz (Mohr and Zipser 1996; Nesbitt et al. 2000) and the TMI operational rainfall product (Del Genio and Kovari 2002). Their results indicate that the vast majority of storms have equivalent radii smaller than 100 km, while our result shows that the RCSL splits into two distinct groups of 10–20 and 100–200 km depending on the storm category. There are two reasons for the discrepancy between the past studies and present work. The first is the same as that already described for cloud clusters. The difference in size between an organized system and an individual element in it is even greater for rainfall since each raining cell is less extensive than a cloud element. The second is due to the truncation by the finite satellite swath. All spaceborne microwave sensors currently fly on LEO, limiting the swath width and hence the size of storms measured by the contiguous pixel method. The CCSL and RCSL, in contrast, are less sensitive to the satellite swath width, as is demonstrated in section 4.

c. Dependence on SST

Del Genio and Kovari (2002) examined the influence of large-scale vertical motion and SST upon storm radius and other storm characteristics based on the data for 1–5 February 1998. They found a significant positive dependence of storm radius on SST when the sample was limited to MCS and a weak positive correlation when all storms were included. This fact is consistent with our results given in section 3, which indicate that *Deep convective* systems exhibit a rapid increase with SST in the probability of occurrence once SSTs exceed 28°–29°C and that *Shallow* events are less sensitive to SST. Furthermore, Fig. 9 of Del Genio and Kovari (2002) indicates that storms occur independently of large-scale vertical motion if SST is warmer than ~28°C, but storms are otherwise capable of developing only when large-scale vertical motion is positive or nearly zero. This supports the 28°–29°C threshold identified from our results (section 3).

6. Summary and conclusions

The characteristics of precipitating cloud systems over the tropical Pacific have been examined in terms of their vertical and horizontal extent using infrared brightness temperature and radar echo-top height. The present study employed TRMM VIRS and PR data during February 1998 and February 2000 for three regions over tropical oceans (west, central, and east Pacific) and two tropical continents (South America and Africa) for comparison. The two time periods adopted correspond to different phases of ENSO: February 1998 experienced the 1997/98 El Niño, while climatic patterns had returned to normal by February 2000 after the La Niña year of 1999.

The height spectrum of tropical convective systems was investigated in terms of infrared T_b and radar echo-top heights. The storm spectrum exhibits a variability consistent with the climatological pattern in tropical rainfall: deep systems are common over the western Pacific warm pool, while shallow convection takes their place in the central and east Pacific in the absence of El Niño. In contrast, rainfall systems frequently develop beyond the freezing level everywhere across the tropical Pacific during the El Niño event in 1998. These systematic variations in the storm spectrum are accounted for by the climatological pattern of the Walker circulation and its ENSO-related change. African rain systems lack the shallow-convection peak and show less ENSO-related variations than the oceanic regions. Precipitation systems over tropical South America have a weak similarity to the oceanic rainfall variability under the influence of a synoptic environmental change.

Four storm categories were defined based on VIRS infrared T_b and PR echo-top height, namely, *Shallow*, *Cumulus congestus*, *Deep stratiform*, and *Deep convective*. The *Shallow* category consists of shallow convection that has a cloud top much warmer than the freezing temperature and an echo-top height below the freezing level. This category contains a distinct group of storms over ocean and accounts for the vast majority of storms in the central and east Pacific in February of a normal year. Cloud-top heights and radar echo-top height can exceed the freezing level but are not high enough to reach the tropopause in the *Cumulus congestus* category. *Cumulus congestus* events constitute a weak but nevertheless distinct peak in the height spectrum of storms in some cases. Both the *Deep stratiform* and *Deep convective* categories represent rain systems with very cold cloud tops. These two categories are differentiated in the way that radar echo-top heights remain near the freezing level for *Deep stratiform* systems, while *Deep convective* events are capable of developing far above the freezing height. A PR echo-top height much higher than the freezing level implies the presence of large ice hydrometeors, which are produced only in deep convection. *Deep convective* events are therefore likely to be found in deep convective cores or

TABLE 4. The percentage of occurrence of each storm category, normalized in each region and year. The uncategorized regimes (blanks in Fig. 1, top; see also section 3) account for the residual percentage (10%–15%) in each column.

	West Pacific		Central Pacific		East Pacific		South America		Africa	
	2000	1998	2000	1998	2000	1998	2000	1998	2000	1998
Shallow	12%	24%	50%	13%	54%	17%	8%	12%	2%	4%
Cumulus congestus	15%	13%	17%	10%	20%	12%	18%	17%	14%	16%
Deep stratiform	32%	20%	8%	31%	7%	27%	33%	27%	25%	28%
Deep convective	27%	31%	15%	32%	8%	29%	28%	30%	49%	42%

their neighborhood, while the *Deep stratiform* category traces the stratiform region far away from the convective region. The probability of occurrence of each storm category in each region and year is summarized in Table 4.

Shallow events generally have the highest probability of occurrence for relatively cold SSTs, while *Deep convective* events show a rapid increase with SST to overwhelm the other storm categories once SSTs are higher than 28° or 29°C. The value of 28°–29°C is a regime-independent SST threshold beyond which deep systems prevail with the exception of the west Pacific in 2000, where *Deep convective* systems dominate over the entire range of SST.

Rain correlation-scale length (RCSL) and cloud correlation-scale length (CCSL) were introduced to assess the horizontal extent of storms. The RCSL (CCSL) is defined based on the expectation of finding rain (clouds) as a function of distance around a given raining point. Compared to conventional approaches where a raining or cloudy area is estimated from contiguous satellite pixels, the RCSL and CCSL represent the size of an entire organized system independent of the contiguity. Moreover, the CSLs are less severely limited by the finite swath width of LEO satellite such as TRMM. The expectation of finding rain declines quickly as distance increases around *Shallow* and *Cumulus congestus* events, while *Deep stratiform* and *Deep convective* systems were found organized over a scale of hundreds of kilometers. Clouds associated with *Shallow* and *Cumulus congestus* storm systems constitute a larger nonprecipitating cloud field instead of a single organized storm system, and hence the CCSL is not defined for those categories. In contrast, clouds are more extensively organized than rainfall around *Deep stratiform* and *Deep convective* systems, indicating that those systems consist of MCSs with extensive cirrus anvils. The qualitative characteristics of storms are summarized in Table 5 for each storm category.

The character of clouds and rainfall associated with *Shallow* and *Cumulus congestus* events does not depend strongly on the time periods or geographical regions analyzed, showing small values of RCSL and CCSL in the range of 8–18 km. On the other hand, the *Deep stratiform* and *Deep convective* categories exhibit significant regional and ENSO-related variations in RCSL and CCSL for oceanic storms. The CCSL shows the most dramatic increase in the central and east Pacific during an El Niño year, reaching up to 500 km. The CCSL/RCSL associated with *Deep stratiform* systems exhibits a coherent variability with that around *Deep convective* events, but the CSLs around *Deep stratiform* systems are consistently larger than those around *Deep convective* ones.

The variability of CCSL leads to an important, controversial issue: how much radiative impact do anvil clouds associated with deep convection have on the earth's energy budget (Del Genio and Kovari 2002, and references therein)? Two hypotheses concerning this issue have been proposed in the context of radiative feedback working between SST and anvil cirrus. The "thermostat" hypothesis (Ramanathan and Collins 1991) states that anvil clouds extend more as the ocean warms up, as opposed to the "adaptive iris" hypothesis (Lindzen et al. 2001) where the warming of SST reduces the cloud fraction. Interestingly, both hypotheses are said to oppose global warming, the first through the increased reflection of incoming shortwave radiation and the second through increased infrared emission to space. Anvil clouds are capable of both heating and cooling the earth depending on the trade-off between the albedo and greenhouse effects. This double-edged nature allowed the conflicting thermostat and iris hypotheses to lead to the same conclusion: the cloud feedback works negatively to suppress an increase in SST. Impacts of the variability in the storm characteristics upon the earth's radiation budget will need to be examined in future work. Studies of that kind are one of

TABLE 5. Summary of storm characteristics for each category. The predominant rain type is defined depending on which of the stratiform or convective rain types dominates relative to their means integrated across all the storm categories (see Table 3).

Storm category	Infrared T_b	Radar echo-top height	Predominant rain type	RCSL	CCSL
Shallow	Warm	Low	Stratiform	Small	N/A
Cumulus congestus	Moderate	Freezinglevel	Convective	Small	N/A
Deep stratiform	Cold	Freezinglevel	Stratiform	Very large	Very large
Deep convective	Cold	High	Convective	Large	Large

the important subjects to which the methodology proposed by this study could be applied.

Acknowledgments. This research is supported by NOAA's Office of Global Programs Grant NA17RJ1228#15 and by NASA's Precipitation Program Grant NAG5-13694. The authors thank W. Berg and A. Rapp for helpful comments and discussions. The TRMM datasets (1B01 and 2A23) were provided by the National Aeronautics and Space Administration (NASA) Goddard Space Flight Center (GSFC). The SST dataset retrieved from TMI was obtained from the Remote Sensing Systems (RSS; at the web Site http://www.ssmi.com/tmi/tmi_browse.html), sponsored by NASA's Earth Science Information Partnerships (ESIP)—a federation of information sites for Earth Science—and by NASA's TRMM Science Team.

REFERENCES

Chen, S. S., R. A. Houze Jr., and B. E. Mapes, 1996: Multiscale variability of deep convection in relation to large-scale circulation in TOGA COARE. *J. Atmos. Sci.,* **53,** 1380–1409.

Del Genio, A. D., and W. Kovari, 2002: Climatic properties of tropical precipitating convection under varying environmental conditions. *J. Climate,* **15,** 2597–2615.

Halverson, J. B., T. Rickenbach, B. Roy, H. Pierce, and E. Williams, 2002: Environmental characteristics of convective systems during TRMM-LBA. *Mon. Wea. Rev.,* **130,** 1493–1509.

Houze, R. A., Jr., 1993: *Cloud Dynamics.* Academic Press, 573 pp.

——, and C.-P. Cheng, 1977: Radar characteristics of tropical convection observed during GATE: Mean properties and trends over the summer season. *Mon. Wea. Rev.,* **105,** 964–980.

Inoue, T., and K. Aonashi, 2000: A comparison of cloud and rainfall information from instantaneous visible and infrared scanner and precipitation radar observations over a frontal zone in east Asia during June 1998. *J. Appl. Meteor.,* **39,** 2292–2301.

Johnson, R. H., T. M. Rickenbach, S. A. Rutledge, P. E. Ciesielski, and W. H. Schubert, 1999: Trimodal characteristics of tropical convection. *J. Climate,* **12,** 2397–2418.

Kummerow, C., W. Barnes, T. Kozu, J. Shiue, and J. Simpson, 1998: The Tropical Rainfall Measuring Mission (TRMM) sensor package. *J. Atmos. Oceanic Technol.,* **15,** 809–817.

Lindzen, R. S., M.-D. Chou, and A. Y. Hou, 2001: Does the earth have an adaptive infrared iris? *Bull. Amer. Meteor. Soc.,* **82,** 417–432.

López, R. E., 1976: The radar characteristics of the cloud populations of tropical disturbances in the northwest Atlantic. *Mon. Wea. Rev.,* **104,** 268–283.

——, 1977: The lognormal distribution and cumulus cloud populations. *Mon. Wea. Rev.,* **105,** 865–872.

Machado, L. A. T., and W. B. Rossow, 1993: Structural characteristics and radiative properties of tropical cloud clusters. *Mon. Wea. Rev.,* **121,** 3234–3260.

——, M. Desbois, and J.-Ph. Duvel, 1992: Structural characteristics of deep convective systems over tropical Africa and the Atlantic ocean. *Mon. Wea. Rev.,* **120,** 392–405.

——, W. B. Rossow, R. L. Guedes, and A. W. Walker, 1998: Life cycle variations of mesoscale convective systems over the Americas. *Mon. Wea. Rev.,* **126,** 1630–1654.

Mapes, B. E., and R. A. Houze Jr., 1993: Cloud clusters and superclusters over the oceanic warm pool. *Mon. Wea. Rev.,* **121,** 1398–1415.

Masunaga, H., T. Iguchi, R. Oki, and M. Kachi, 2002: Comparison of rainfall products from TRMM Microwave Imager and Precipitation Radar. *J. Appl. Meteor.,* **41,** 849–862.

Mohr, K. I., and E. J. Zipser, 1996: Mesoscale convective systems defined by their 85-GHz ice scattering signature: Size and intensity comparison over tropical oceans and continents. *Mon. Wea. Rev.,* **124,** 2417–2437.

Nesbitt, S. W., E. J. Zipser, and D. J. Cecil, 2000: A census of precipitation features in the Tropics using TRMM: Radar, ice scattering, and lightning observations. *J. Climate,* **13,** 4087–4106.

Petersen, W. A., S. W. Nesbitt, R. J. Blakeslee, R. Cifelli, P. Hein, and S. A. Rutledge, 2002: TRMM observations of intraseasonal variability in convective regimes over the Amazon. *J. Climate,* **15,** 1278–1294.

Ramanathan, V., and W. Collins, 1991: Thermodynamic regulation of ocean warming by cirrus clouds deduced from observations of the 1987 El Niño. *Nature,* **351,** 27–32.

Rickenbach, T. M., and S. A. Rutledge, 1998: Convection in TOGA COARE: Horizontal scale, morphology, and rainfall production. *J. Atmos. Sci.,* **55,** 2715–2729.

Schumacher, C., and R. A. Houze Jr., 2003: The TRMM precipitation radar's view of shallow, isolated rain. *J. Appl. Meteor.,* **42,** 1519–1524.

Short, D. A., and K. Nakamura, 2000: TRMM radar observations of shallow precipitation over the tropical oceans. *J. Climate,* **13,** 4107–4124.

Takayabu, Y. N., 2002: Spectral representation of rain profiles and diurnal variations observed with TRMM PR over the equatorial area. *Geophys. Res. Lett.,* **29,** 1584, doi:10.1029/2001GL014113.

TRMM PR Team, 2000: Tropical Rainfall Measuring Mission (TRMM) precipitation radar algorithm instruction manual Version 2.0. NASDA/NASA, 115 pp. [Available online at http://www.eorc.jaxa.jp/TRMM/document/pr_manual/pr_manual2.pdf.]

Williams, E., and Coauthors, 2002: Contrasting convective regimes over the Amazon: Implications for cloud electrification. *J. Geophys. Res.,* **107,** 8082, doi:10.1029/2001JD000380.

Williams, M., and R. A. Houze Jr., 1987: Satellite-observed characteristics of winter monsoon cloud clusters. *Mon. Wea. Rev.,* **115,** 505–519.